Acta Materialia 200 (2020) 1008–1021

Contents lists available at ScienceDirect

Acta Materialia

journal homepage: www.elsevier.com/locate/actamat

Full length article

Ultrahigh temperature *in situ* transmission electron microscopy based bicrystal coble creep in Zirconia II: Interfacial thermodynamics and transport mechanisms

Robson L. Grosso[a,b,c], K.S.N. Vikrant[d], Lin Feng[e], Eliana N.S. Muccillo[b], Dereck N.F. Muche[c], Gowtham S. Jawaharram[a], Christopher M. Barr[e], Anthony M. Monterrosa[f], Ricardo H.R. Castro[c], R. Edwin García[d], Khalid Hattar[f], Shen J. Dillon[a,*]

[a] Department of Materials Science and Engineering, University of Illinois Urbana-Champaign, Urbana, IL61801, United States
[b] Energy and Nuclear Research Institute, PO Box 11049, S. Paulo, Brazil
[c] Department of Materials Science and Engineering, University of California - Davis, California 95616, United States
[d] School of Materials Engineering, Purdue University, West Lafayette, IN47907, United States
[e] School of Chemical Engineering and Technology, Sun Yat-sen University, Zhuhai 519082, China
[f] Materials, Physical, and Chemical Sciences, Sandia National Laboratories, Albuquerque, NM87185, United States

ARTICLE INFO

Article history:
Received 17 February 2020
Revised 12 July 2020
Accepted 24 August 2020
Available online 28 August 2020

ABSTRACT

This work uses a combination of stress dependent single grain boundary Coble creep and zero-creep experiments to measure interfacial energies, along with grain boundary point defect formation and migration volumes in cubic ZrO_2. These data, along with interfacial diffusivities measured in a companion paper are then applied to analyzing two-particle sintering. The analysis presented indicates that the large activation volume, $v_* = v^f + v^m$ primarily derives from a large migration volume and suggests that the grain boundary rate limiting defects are delocalized, possibly due to electrostatic interactions between charge compensating defects. The discrete nature of the sintering and creep process observed in the small-scale experiments supports the hypothesis that grain boundary dislocations serve as sources and sinks for grain boundary point defects and facilitate strain during sintering and Coble creep. Model two-particle sintering experiments demonstrate that initial-stage densification follows interface reaction rate-limited kinetics.

1. Introduction

Oxide grain boundaries remain rather enigmatic microstructural features. Although much is known about the structure, properties, and distributions of these interfaces, large knowledge gaps remain in our understanding of their transport mechanisms and thermodynamics [1–5]. In most oxides, considerable disagreement remains regarding the fundamental transport mechanisms that give rise to kinetic processes such as diffusion, densification, creep, or grain growth [6–19]. In fact, little is known about the nature of transport mediating defects in oxides interfaces. The need for an improved fundamental understanding of interfacial transport processes has also become apparent with the emergence of novel sintering methods [20–22]. The application of rapid heating rates and short sintering times at high temperatures, often called fast sintering, has been known for three decades to be effective in promoting densification relative to coarsening [23]. The mechanisms associated with novel high heating rate processing methods, such as microwave sintering, spark plasma sintering, and flash sintering have been the subject of considerable debate [9,20,22,24–28]. The effects of manipulating field variables cannot be discounted as having an effect, but recently demonstrated rapid heating methods show that the rapid heating itself can explain much of the enhanced sintering associated with these processes [26]. Other recent rapid heating experiments on ZnO [27] and 3YSZ [28] without an applied external electric field also achieved rapid densification rates similar to flash sintered samples indicating that the heating rate is a key factor in promoting rapid densification sintering.

The classic explanation for the efficacy of fast sintering assumes that the activation energy for surface diffusion, which mediates coarsening, and grain boundary diffusion, which mediates densification, differ by an amount sufficient to influence the dominant mechanism. [23] The results for ZrO_2 in the companion paper [29] demonstrate that little difference exists between the activation energies for surface diffusion and grain boundary diffu-

* Corresponding author.
E-mail address: sdillon@illinois.edu (S.J. Dillon).

https://doi.org/10.1016/j.actamat.2020.08.070
1359-6454/

sion in this system. ZrO_2 can, nevertheless, be sintered effectively using fast sintering methods [20,30,31]. Classical sintering models only contain differing temperature dependencies in the diffusion and the interfacial energy terms. The interfacial energies are generally expected to have a weak temperature dependence, at fixed composition, over a temperature change of several hundred degrees, which is on the order of the temperature differences relevant to fast sintering versus conventional sintering. Particle rearrangement in the initial stages of sintering has also been suggested to have a potential effect relevant to heating rates and sintering temperatures, but has not been systematically quantified [32]. Since fast sintering methods are effective in a broad range of systems, a new mechanistic understanding of the temperature dependence of sintering likely needs to be developed to sufficiently rationalize the phenomenon.

Grain boundary diffusion mediated densification generally results from a point defect flux along the boundary that removes atoms from it [33]. This could either be facilitated by a vacancy flux from the surface or an interstitial flux to the surface. The surface functions as a nearly perfect sink for point defects, but the boundary must also have sources and sinks for the grain boundary point defects. Interfacial dislocations can serve as point defect sources and sinks, analogous to how dislocations can be point defect sources and sinks in the lattice [34–37]. A continuous flux of point defects from the lattice to appropriate grain boundary dislocations (GBD) has been shown, during irradiation, to be accommodated via climb of those GBDs [37]. For example, disconnections are a grain boundary dislocation that have both a step height and burgers vector. If the burgers vector is in the plane of the boundary it can glide and if it is out of the grain boundary plane it must climb [38]. Under stress, this climb can be biased to induce creep or sintering. GBDs should similarly act as sources and sinks for grain boundary point defects that tend to dominate Coble creep and sintering. The sintering stress imposes a stress gradient between the source and sink. The creation and annihilation of point defects at different stresses leads to dissipation of energy in proportion to the formation volume of the defect. The reduction in interfacial energy during sintering provides the driving force for this dissipative process. If densification is indeed mediated by GBDs, then the process could be discrete when grain boundary neck widths are sufficiently small to only support a single densification mediating GBD. Furthermore, since the removal of a layer of atoms from a grain boundary neck by the proposed mechanism should proceed by the nucleation, propagation, and eventual annihilation of a GBD, it follows that both GBD nucleation kinetics and the energy barrier to densification should play an important role in the overall densification kinetics. In fact, several researchers have suggested that interface reaction-rate limited kinetics could be important in sintering, but the experimental evidence is limited [39,40]. Reaction rate limited kinetics generally follow Arrhenius behavior independent of the Arrhenius nature of the underlying diffusivity. This creates the possibility that densification and coarsening mechanisms have very different activation energies, despite the fact that the grain boundary and surface diffusivities that mediated the processes may have similar activation energies. Gaining new fundamental insights into the complex phenomena of sintering and creep requires the development of holistic experimental and computational methodologies that provide mechanistic data while decoupling four dominant effects in microstructural evolution: thermodynamic driving forces, transport kinetics along competing paths, transport mechanisms, and microstructural topology effects.

In order to quantitatively analyze the thermodynamics and kinetics of sintering it is valuable to have reliable measures of interfacial diffusivities, interfacial energies, and transport mechanisms. Point defect activation, formation, and migration volumes provide insights into the nature of the diffusion mediating defect and are a cornerstone of understanding fundamental aspects of diffusion. Grain boundary activation volumes have only been measured in several metals [41,42]. Grain boundary defect formation volumes, to the authors' knowledge, have not been experimentally measured in any material systems. Grain boundary diffusion in oxides could result from various mechanisms ranging from the migration of individual point defects, to collective motion of species, to the motion of GBDs [18,43,44]. It has been suggested that the delocalized nature of point defects in oxide grain boundaries may account for anomalous grain boundary diffusion observed in certain systems [18]. Recent atomistic simulations in MgO also suggest that point defects in twist boundaries tend to delocalize [45]. Observing such effects, or even their consequences, in traditional experiments is unfeasible.

The activation volume for diffusion may be measured from pressure dependent grain boundary diffusivity [46]. Tracer diffusion is typically employed for grain boundary diffusivity determination but is too laborious for the investigation envisioned herein. The formation volume may be determined from the effect of pressure on the energy dissipated during point defect formation. Bicrystal Coble creep experiments provide a means for measuring grain boundary diffusivity [44]. The related zero-creep experiment typically applied to wires with 'bamboo' grain structures, i.e. a series of bicrystals, provides a measure of interfacial energy [47,48]. The zero-creep experiment finds the force above which tensile creep occurs in a thin wire and below which densification occurs. This applied force, i.e. the zero-creep force, balances the capillarity and allows for the measure of surface energy. Since these experiments can be readily performed as a function of stress, a combination of kinetic measurements via bicrystalline creep and thermodynamic measurements through the zero-creep analysis provide the basis for measuring grain boundary diffusivity as well as the defect formation and migration volumes. Bicrystal creep and zero-creep methods, however, have not generally been applied to oxides and brittle crystalline materials that are difficult to prepare as thin wires having bamboo grain structures and equally difficult to mechanically test at high homologous temperatures.

The companion paper [29] to this developed a high temperature *in situ* transmission electron microscopy (TEM) based nanomechanical testing scheme for measuring interfacial diffusion during single grain boundary Coble creep [29]. The current work focuses on measuring interfacial energies along with grain boundary diffusion mediating point defect migration, formation, and activation volumes and their relative entropic and enthalpic contributions in cubic ZrO_2. The sign of the point defect formation volume and large migration volume suggest the grain boundary diffusion mediating point defects are vacancy-type. Both the creep and sintering experiments suggest that these processes are both mediated by GBDs acting as point defect sources and sinks. The model two-particle sintering data suggest that a barrier to densification indeed exists causing reaction-rate limited kinetics, at least for the sub-micron particles characterized.

2. Experimental procedure

The details of sample preparation are provided in the companion paper and are summarized briefly here [29]. Dense 10%Sc_2O_3 doped ZrO_2 (10ScSZ) samples were prepared following a procedure detailed elsewhere [49,50]. Pre-annealing of focused ion beam prepared nanopillars was performed via *in situ* using laser heating at T $\approx$ 2000 °C for ≈15 min. In the process, the grain size coarsened to d>20 μm, the nanopillar geometry relaxed via capillarity effects, and the resulting test specimen were in single crystalline asperities. Ga_2O_3 evaporates at $T_{boil} \approx$ 1900 °C, leading us to anticipate little residual contamination from focused ion beam preparation. A

≈ 100 μm diameter 1064 nm 20 W laser was used to heat the sample. Temperature calibration was based on a combination of electron diffraction based thermal expansion measurements, which show linear laser power-temperature response, and reference temperature values at phase transitions occurring in the system. Calibration curves are shown in Figure S1.

Two sample sets were investigated; 10ScSZ asperities were sintered *in situ* to an 8%Y_2O_3 doped ZrO_2 (8YSZ) single crystal, and a second set of experiments sintered two 10ScSZ samples together. The samples will be referred to as YSZ-ScSZ and ScSZ-ScSZ, respectively. The YSZ-ScSZ based bicrystal formed a random high-angle type boundary with a misorientation of 21 º about the [1 $\bar{1}$ 16]; as measured by electron diffraction. The ScSZ-ScSZ experiments measured random grain boundary misorientations formed at different locations along the polycrystalline sample.

Experiments were performed in a 200 kV JEOL 2100 using a Bruker PI-95 picoindenter. Two types of experiment were performed; one in which the sample was allowed to sinter and form a relatively large grain boundary neck for > 30 s prior to tensile loading, i.e. YSZ-ScSZ experiments, and one in which tensile loading was applied just after contact such that limited neck growth occurred; the ScSZ-ScSZ experiments. The large neck allows for accurate measurement of the stress-strain response. Constant displacement experiments were performed at rates between 0.5 nm s^{-1} and 1000 nm s^{-1} and constant load experiments were performed at loads varying between 2 μN and 150 μN. The precision of the instrument is ≈ 0.4 μN and the accuracy is ≈ 1 μN. The laser repetition rate, 33 kHz, is fast relative to the thermal relaxation time of the sample, due to its high thermal impedance. Steady-state sample temperature was obtained at timescales on the order of 10 minutes. An *in situ* image acquisition rate of ≈ 15 Hz (Tietz video and image processing system) was used. The threshold for electron displacement damage in ZrO_2 has been measured to be ≈ 1 MeV, [51] which is significantly lower than the 200 keV used here. Electron beam heating is similarly anticipated to be negligible. Images were analyzed using ImageJ. The areas, lengths, and geometric alignment of particles were measured using ellipse split in ImageJ [52]. The mean widths of particles were determined using imagej by finding the perimeter of the convex hulls bounding them dividing by π. Dihedral angles were measured manually from the surface tangents observed at the grain boundary necks using imagej.

Phase-field simulations were performed in the companion paper [29]. Some aspects of the results will be discussed only briefly here, and the reader is referred to that manuscript for details.

3. Results and discussion

3.1. Mechanical response and GB transport mechanism under stress

Fig. 1 plots the load-displacement response of YSZ-ScSZ samples tested with different loading rates at 1928 °C. The *in situ* videos associated with experiments performed at each rate are provided in Videos S1-S6. The mechanical response is rate sensitive, and plastic deformation is observed at lower rates. Plasticity is manifest as load drops observed in the load-displacement curves. At higher loading rates, the samples load elastically until the onset of brittle failure. The yielding occurs at stresses < 50% of the single crystal compressive yield strength in all cases, at <25% of the compressive yield strength at similar tensile versus compressive strain rates, and <3% of the bulk yield strength at the lowest strain rates [53]. Since plasticity occurs at <3% of the bulk yield strength it is anticipated to result from creep. The example shown at 1928 °C demonstrates that during testing at 1 nm s^{-1} the sample no longer fractures, but instead undergoes a series of such load drops. The associated time-lapse images indicate that the sample geometry under this condition is effectively constant (see Figure S2). This general phenomenon was observed at all temperatures examined. Fig. 2 plots the natural log of the strain rate, $ln\dot{\varepsilon}$, versus the yield stress,σ_y, at several temperatures, which demonstrates the broad range of conditions over which the phenomena were observed. There are two regimes in the plot, i.e. brittle fracture and yielding, that are noted by the dashed line. No slip, plastic deformation, or fracture is observed in the bulk lattice. Samples also fracture after yielding, but these samples do not display any discernable strain rate dependence of fracture stress and have an average fracture strength of ≈ 500 MPa. Discrete load drops are commonly observed in nanomechanical tests associated with plastic events [54]. The load drops in our experiments, however, exhibit relatively large time constants. Furthermore, they are observed at sample loading rates too large to be associated with drift of the indenter; i.e. drift rates are typically < 1 nm s^{-1}. The discrete creep response, lack of bulk plasticity, and rate dependence motivate our hypothesis that the grain boundary plasticity is diffusion mediated; e.g. a point defect flux to and from GBDs that mediates their growth or recession, as discussed in more detail below. Cubic ZrO_2 grain boundaries have been thoroughly characterized by high-resolution TEM and are generally found to contain GBDs that could at as point defect sources and sinks [55,56].

To test the hypothesis that diffusion mediated GBD motion accounts for the observed load drops, the time constants associated with the load drops were used to calculate diffusivities following;

$$D_{gb} = {x^2 RT}/{2\pi t_c \sigma V_m} \quad (1)$$

Here, R is the gas constant, T is temperature, σ is the stress,$V_m$is the molar volume, x is the grain boundary neck width, and t_c, is the time constant associated with inserting a single atomic plane into the grain boundary neck. An example measurement of t_c is shown in Figure S3. The results are plotted in Fig. 3 along with data obtained from the 'nanowire-growth' single grain boundary Coble experiments described in the companion paper [29]. These disparate data sets agree well, which suggests that the load drops are indeed associated with the same grain boundary diffusional process that mediates the growth of the nanowire-like features. These experiments were originally intended to approach the zero-creep condition via displacement control and measure the associated stress. However, even as the average load approaches zero, significant oscillations persist; see example in Figure S4.

At an average stress of ≈ 0, the stress oscillates between tensile and compressive values of ≈ 20-35 MPa. Elastic finite element simulations of strains induced by a length change of ≈ 1 Burger's vector produce a similar level of stress ≈ 20 MPa; see Figure S5. These values are of similar magnitude, but the total stress change associated with these hysteresis loops is ≈ 40-70 MPa. It is not unreasonable to expect that these loops could be associated with the insertion and removal of atomic planes with a step height of ≈ $2\vec{b}$ or ≈1 a_o. In fact, surface steps tend to be on the order of 1-2 $\vec{b}$ or 1 a_o, depending which minimizes interfacial energy [57,58]. Furthermore, grain boundary steps accompanying GBDs in ZrO_2 have been observed to be larger than 1 $\vec{b}$ in certain boundaries. At this length scale the continuum nature of the zero-creep model breaks down since nucleation of a GBD induces a discreet displacement. The oscillations in load are hypothesized to reflect the discrete nature of an atomic step being added to or removed from the grain boundary. Burton [59] originally proposed a GBD mechanism for creep described as being mediated by 'grain boundary dislocation climb sources'. The model, however, was discussed in the context of Nabarro-Herring creep rather than Coble creep and interface reaction rate limiting kinetics. More generalized creep models incorporating GBDs or grain boundary sources and sinks have more recently been described, which can capture both diffusion-limited

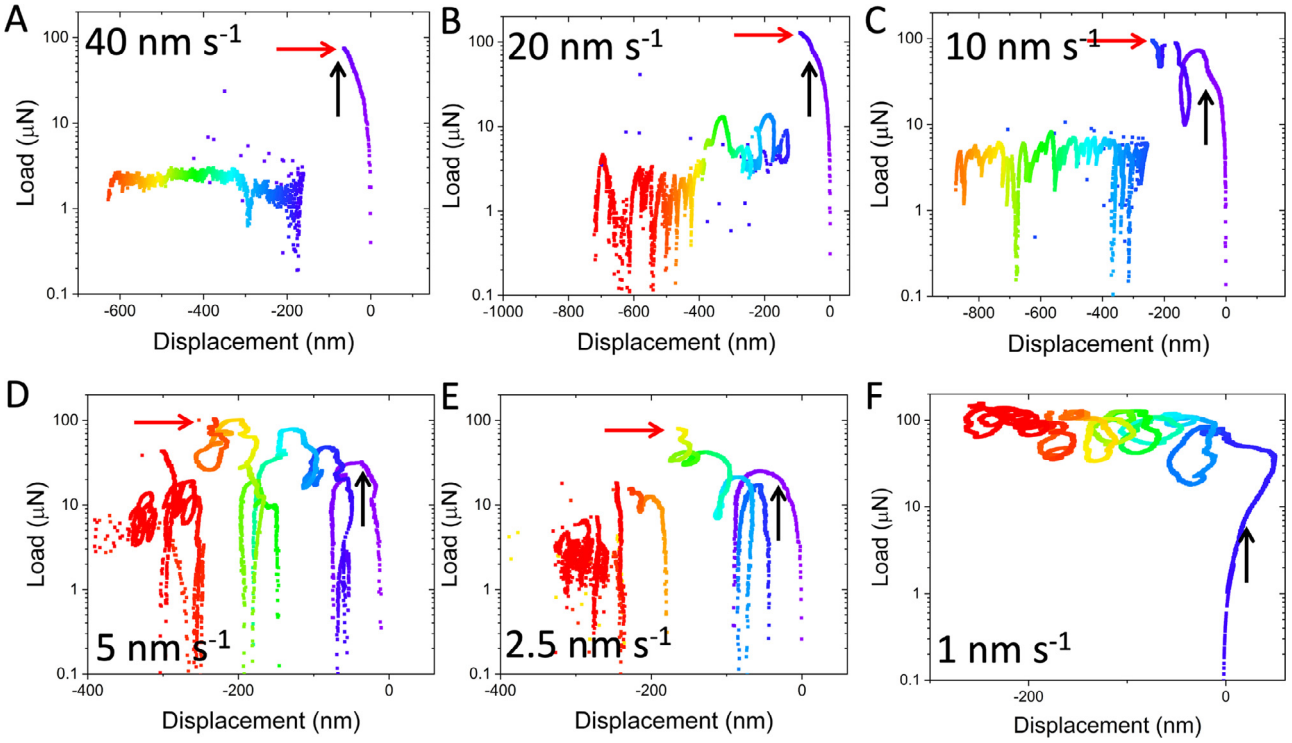

Fig. 1. A-F Representative load-displacement curves for YSZ-ScSZ samples tested at different displacement rates at 1928 °C. The fracture loads are noted by red arrows and the yielding behavior is highlighted by black arrows. The color scale represents time where purple is zero time and red is the final time.

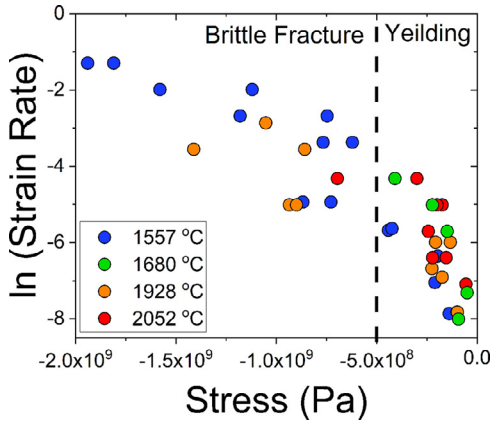

Fig. 2. The natural log of the strain rate versus yield or fracture stress, whichever occurs earliest, plotted for different temperatures. The slopes in the yielding regime are fit to measure the activation volume as a function to temperature.

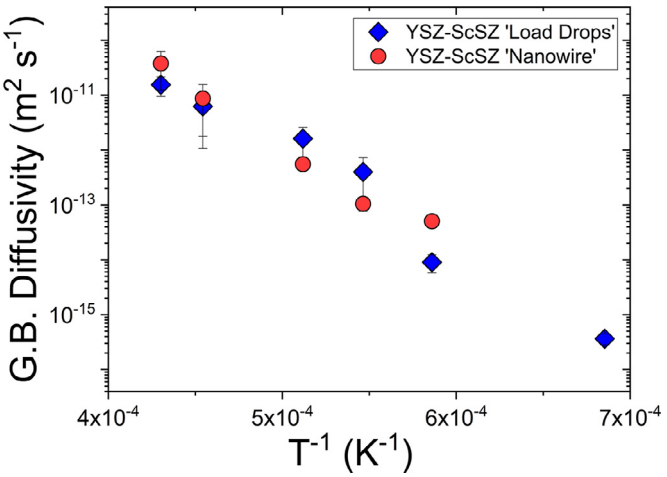

Fig. 3. The time constants associated with the load drops in the load-displacement curves are used to calculate diffusivities. Grain boundary diffusivities are shown on an Arrhenius plot along with values for the same YSZ-ScSZ samples determined from the growth of nanowire-like features discussed in the companion paper [29]. The agreement between these two sets of experiments indicates that the load drops are mediated by the same diffusional process controlling the nanowire growth in the bicrystal Coble creep experiments.

and interface reaction rate-limited kinetics, along with appropriate stress, temperature, and grain size dependencies [60–62]. The discrete nature of diffusion mediated grain boundary plasticity is generally consistent with such physical mechanisms.

The activation volume, v^*, associated with plasticity may be determined from the relation $v^* = -kT\frac{dln\dot{\varepsilon}}{d\sigma}$, where k is Boltzmann's constant, $\dot{\varepsilon}$ is strain rate, and σ is the yield or flow stress. Often this analysis is applied to the flow stress to treat the steady-state dislocation structure during deformation [63,64]. Our interest here, however, relates to the formation of an initial defect and thus the yield stress is considered. For reference, Fig. 2 plots $ln\dot{\varepsilon}$ versusσ_y at several temperatures. Averaged over temperatures between 1557 °C and 2052 °C, $v^* = 5.2\vec{b}^3 \pm 1.4\vec{b}^3$, where $\vec{b}$ is the lattice Burger's vector, $\frac{1}{2}\langle 110\rangle$. The temperature dependence of the activation volume was determined to be;$\beta^* = -\frac{1}{v^*}(\frac{\partial v^*}{\partial T})_P = 7.1x10^{-3}K^{-1} \pm 2.5x10^{-3}K^{-1}$.

For vacancy mediated lattice diffusion in simple metals $v^* \approx 0.03\vec{b}^3 - 0.07\vec{b}^3$, for interstitial diffusion $v^* \approx 0.1\vec{b}^3 - 0.3\vec{b}^3$ and for plasticity in crystals, single crystal pillars tested in compression, and slip across grain boundaries $v^* \approx 10\vec{b}^3 - 500\vec{b}^3$ [65–74]. Values on the order of $v^* \approx 1\vec{b}^3 - 10\vec{b}^3$ have been measured for dislocation nucleation from surfaces and simulations of polycrystalline creep mediated by mixed grain boundary mechanisms [75,76]. The measurements of $v^* = 5.2\vec{b}^3 \pm 1.4\vec{b}^3$ in this work agrees in magnitude

most closely with a diffusional mechanism. The calculated grain boundary diffusivities associated with the load drop events support the hypothesis of a diffusion dependent mechanism for this process. The values are far too large, however, to associate with an isolated point defect. In order, to better understand the nature of the diffusion mediating defect, the defect formation volume is determined below.

3.2. Surface and grain boundary energies

Cannon and Carter [77] originally provided an exact solution to the zero-creep condition by noting that the magnitude of the sintering potential, Σ, they derived is equivalent to the zero-creep force, $\Sigma = -F$, i.e. the force required to stop sintering. The sintering potential was defined as;

$$\Sigma = \gamma_S\left(2\pi r\cos\varphi - K\pi r^2\right) \tag{5}$$

where K is the surface curvature and φ is the turning angle at the triple junction, which is the angle between the tangent to the surface and the grain boundary plane, and r is the radius of the grain. Josell [47] rederived a solution in the context of the zero-creep experiment used to determine surface energy;

$$\frac{F}{\pi r\kappa} = \gamma_s \tag{2}$$

where $\kappa = 1 - \frac{\gamma_{gb}/\gamma_s}{2L/r}$, F is the force, γ_{gb} is the grain boundary energy, γ_s is the surface energy, and $2L$ in the spacing between grain boundaries along the axis of the sample; here taken here to be the average grain size of the sample. The latter formulation by Josell is used here since it provides a simplified approximation of curvature in an axially symmetric geometry in local equilibrium. If dihedral angles along the length of the asperity contact were visible, then L was measured from the spacing between the grain boundaries. Otherwise, L was taken as the average grain size of the sample measured from *ex situ* SEM images. Fig. 4a-b show a time-lapse image sequence from an example experiment and the associated load, displacement, and neck width versus time curves. The displacement versus time values shown are obtained directly from the micromechanical tester, but it should be noted that displacements were also measured from stable reference points in the image to ensure that any drift in the instrumentation at low displacement rates did not affect the analysis. γ_{gb}/γ_s may be reasonably approximated using the Herring condition [78] applied to the surface triple junction under the assumption of local equilibrium;

$$\gamma_{gb}/\gamma_s = 2\cos\left(\frac{\Theta}{2}\right) \tag{3}$$

where Θ is the dihedral angle. Dihedral angle measurements were obtained from the constant displacement experiments described above, by measuring the angle at the grain boundary necks. Figure S6 shows an example measurement of a set of dihedral angles from both sides of the grain boundary as a function of time. Some variation in angle occurs around specific points in time where the load and grain boundary area changes rapidly, but the average of the two values is reasonably constant throughout the experiment. All measurements of dihedral angle presented represent a measure of both sides of the grain boundary averaged together over several different points in time. Measurements were only made when the grain boundary was oriented approximately perpendicular to the loading axis. No measurable displacement rate dependence of the dihedral angles was observed, and as shown in Fig. 4c no significant trend occurred as a function of temperature. The average dihedral angle was 103 °± 17 °. The dihedral angles agree with equilibrium values calculated in the phase field model, 102 °, discussed in the companion paper [29]. Prior measurements of YSZ dihedral angles have been made from interferometry [79]. The interferometry experiments measured angles in the far field, which likely caused the dihedral angles to be overestimated, and larger than those measured more locally in this work; see Θ_1 in Figure S6 for an example of how the angle at the neck differs from that farther away. Due to the small radius of the neck relative to the grain size, most experiments produced values of $\kappa \approx 0.8 - 0.99$, although several exceptions exist in the data.

A series of constant load experiments were performed by holding the sample at a single load for 5 min and then ramping to a different load and again holding for 5 min. Fig. 4 shows an example time-lapse sequence of images along with load, displacement, and neck radius versus time curves. The neck radius grows continuously, presumably through a combination of surface and grain boundary diffusion. Over specific intervals, where displacement rate is approximately steady state i.e. ≈ 2-5 mins, the volumetric rate of growth or shrinkage of the feature is measured by calculating the product of the displacement rate and the average circumference of the neck. The results of a series of experiments performed at 1975 °C and 2098 °C are plotted in Fig. 4d. These data are fit by a linear function and the y-intercept is taken to be the zero-creep value. At the zero-creep condition the surface energies are determined to be $\gamma_s = 1.32 \pm 0.13$ J m^{-2} and $\gamma_s = 1.35 \pm 0.12$ J m^{-2}, respectively. The error is large relative to the difference between the two temperatures, as expected since the temperature dependence is anticipated to be weak. Much of the scatter in the data in Fig. 4d likely derives from the following: the zero-creep condition is constant regardless of radius, but the slope of $\frac{F}{\pi r\kappa}$ versus $\dot{\varepsilon}$ will depend on r since the energy dissipated is found to be the sum of the interfacial area created plus an additional work term that is linear in stress. The stress dependent work is described in detail below in context of the defect formation volume. Since the interfacial energy term is dominant in this sum, the approach still provides a useful value with a reasonable experimental error. The two results are averaged for further discussion below, $\gamma_s = 1.34 \pm 0.13$ J m^{-2} and have been used for capillarity related calculations throughout this manuscript. Applying the Herring condition results in an average value of $\gamma_{gb} = 1.67$ J m^{-2}. The Herring condition is, of course, an approximation and this analysis also assumes that all dihedral angles measured are in local equilibrium, which is difficult to assess in the creep experiments.

Calorimetric measurements of hydrous 10ScSZ, hydrous 8YSZ, and anhydrous 8YSZ surface energies produce values of 0.75 J m^{-2}, 1.02 J m^{-2}, and 1.32 J m^{-2}, respectively [49,80]. Other authors also measured the surface energy of 8YSZ to be between 1.12 J m^{-2} and 1.25 J m^{-2} [79]. The surface energies measured via calorimetry are sensitive to surface adsorption by species like water that lower the surface energy. Our experiments performed in vacuum at 1975 °C and 2098 °C under electron imaging, which will also displace surface hydroxyls, should be anhydrous. Our results agree reasonably well with measurements of anhydrous YSZ. To the authors' knowledge, no similar measurements of anhydrous ScSZ are available.

3.3. Defect formation volume and the mechanism of bicrystal coble creep

In order to better understand the species mediating grain boundary diffusion, the stress dependences of the work and kinetics of Coble creep are analyzed. The creep process is inherently irreversible and dissipative as indicated by the load-displacement curves. The growth of the nanowire-like structures can dissipate energy by surface diffusion to the neck, nucleation of a new GBDs, elongation of this linear defect as it propagates across the neck, internal friction associated with forcing this defect through the grain boundary, redistribution of chemical species, and formation of new surface. All of these terms will contribute to energy dissipation,

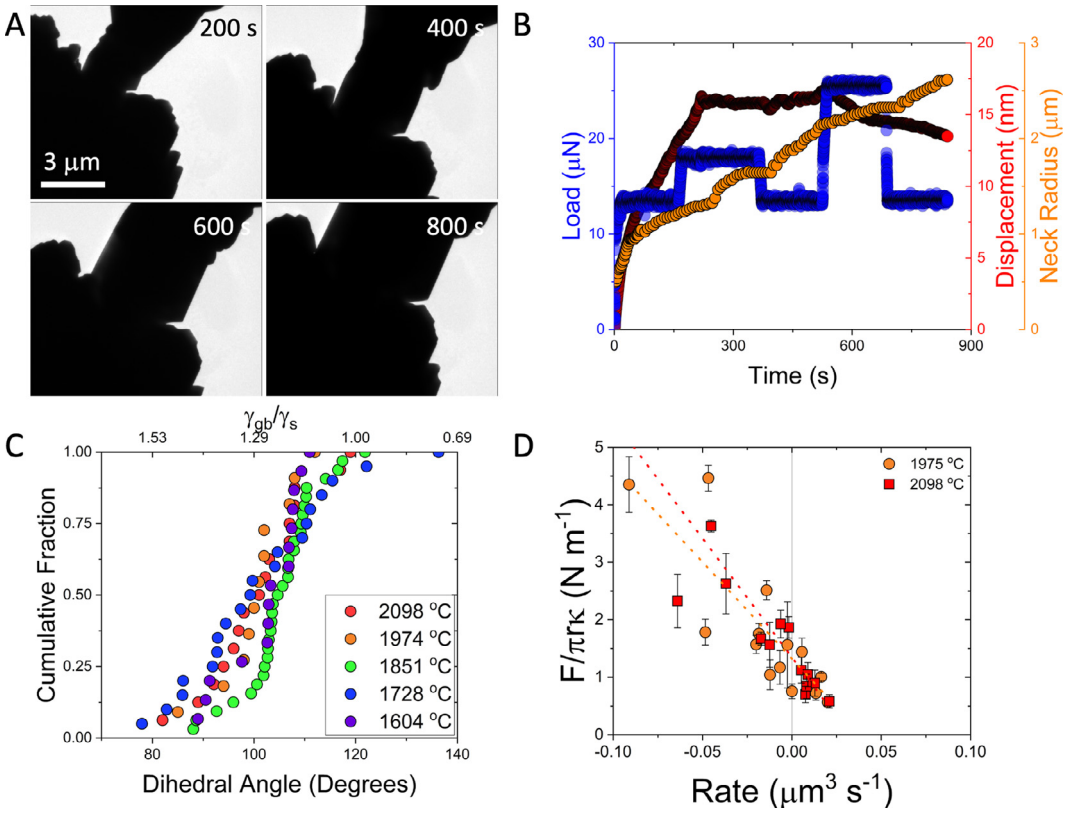

Fig. 4. A) Time-lapse image set of the sample evolution during constant load ScSZ-ScSZ experiments. B) the load, displacement, and neck radius plotted as a function of time for the example experiment shown in A. C) Dihedral angle distribution measured form the ScSZ-ScSZ experiments at different temperatures. D) The energy dissipated per unit surface area during constant tensile load experiments versus volumetric growth rate, where the value at the zero rate is a measure of the surface energy.

but two are anticipated to be dominant. First, the creation of new surface area is the primary source of energy dissipation at lower displacement rates or stresses. Surface diffusion is discounted as a primary energy dissipation mechanism here, because it is not expected to be rate limiting, the surface stress gradient is likely small, and the surface stress-surface point defect coupling is likely to be relatively weak. Any chemical redistribution is anticipated to be transient under our experimental conditions. If nucleation of GBDs or the increase in GBD line energy as it propagates across the approximately cylindrical cross section dissipates the most energy, then the excess energy per unit surface area evolved would scale linearly with displacement rate; i.e. scaling with each new atomic plane created in the grain boundary. The data, however, do not fit this trend well. Plotting energy per atom diffusing into the grain boundary versus pressure provides a more monotonic trend. The difference in these quantities arises from the fact that experiments were performed under conditions of different neck radius. Furthermore, as noted above, the average stress associated with this hysteretic process near the zero-creep conditions is ≈ 40-70 MPa. If GBD nucleation were the primary energy dissipation mechanism, i.e. assuming nucleation hysteresis dissipates all of the excess energy after subtracting the surface contribution, then the activation volume for the nucleation event would be on the order of $v^* \approx 500\vec{b}^3$. Although, reasonable in magnitude relative to dislocation nucleation mechanisms, a value of $v^* \approx 5.2\vec{b}^3$ was already directly determined from our experiments as a function of strain rate.

As discussed above, diffusional transport in the grain boundary is hypothesized to primarily account for the dissipation of energy in excess of the surface energy. For example, the existence of a stress dependent energy barrier at zero applied load indicates that the GBD mediated densification process is inherently coupled to stress. The excess work dissipated per volume, $\frac{dw}{dV}$, of new material entering the grain boundary during constant load experiments was calculated as follows;

$$\frac{dw}{dV} = \left(\frac{F}{\pi x \kappa} - \gamma_s\right)\frac{dA_s}{dt}/\frac{dV}{dt} \tag{4}$$

where A_s is the new free surface area created. Data where the neck width, x, varied significantly during the interval measured were excluded from the analysis, since the value dV is intended to represent a change in volume primarily due to tensile load driven grain boundary diffusion rather than surface diffusion. Fig. 5 demonstrates a linear relationship between stress and the work dissipated per mole of ZrO_2, calculated by $\frac{dw}{dn} = \frac{dV}{dn}\frac{dw}{dV}$ where $\Omega = \frac{dV}{dn}$ is the molecular volume of cubic ZrO_2. Under tension, vacancy type defects could flow from the GBD to the surface and interstitial type defects could flow in the opposite direction. The total energy dissipation via diffusional hopping is assumed here to be small relative to the formation and annihilation of point defects. The total work, w, is thus assumed to follow $\delta w = v^f dP$, where $v^f$is the defect formation volume. From the average slope in Fig. 5, $v^f = 5.0x10^{-3}\vec{b}^3 \pm 2.0x10^{-3}\vec{b}^3$ and $v^f = 3.5x10^{-3}\vec{b}^3 \pm 0.6x10^{-3}\vec{b}^3$ at 1975 °C and 2098 °C, respectively, and an average value of $4.3x10^{-3}\vec{b}^3$ will be used for subsequent discussion. The experiment explicitly determines a volumetric activation strain that is on average ≈ 0.5Ω ± 0.2Ω, where Ω is the molar volume. The positive formation volume suggests the diffusion mediating defect is of a vacancy type. The assumption made above, is that all work performed during single grain boundary Coble creep results from the production of vacancies. If other effects dissipate energy to a significant extent, then our measurement of v^f represents an upper bound.

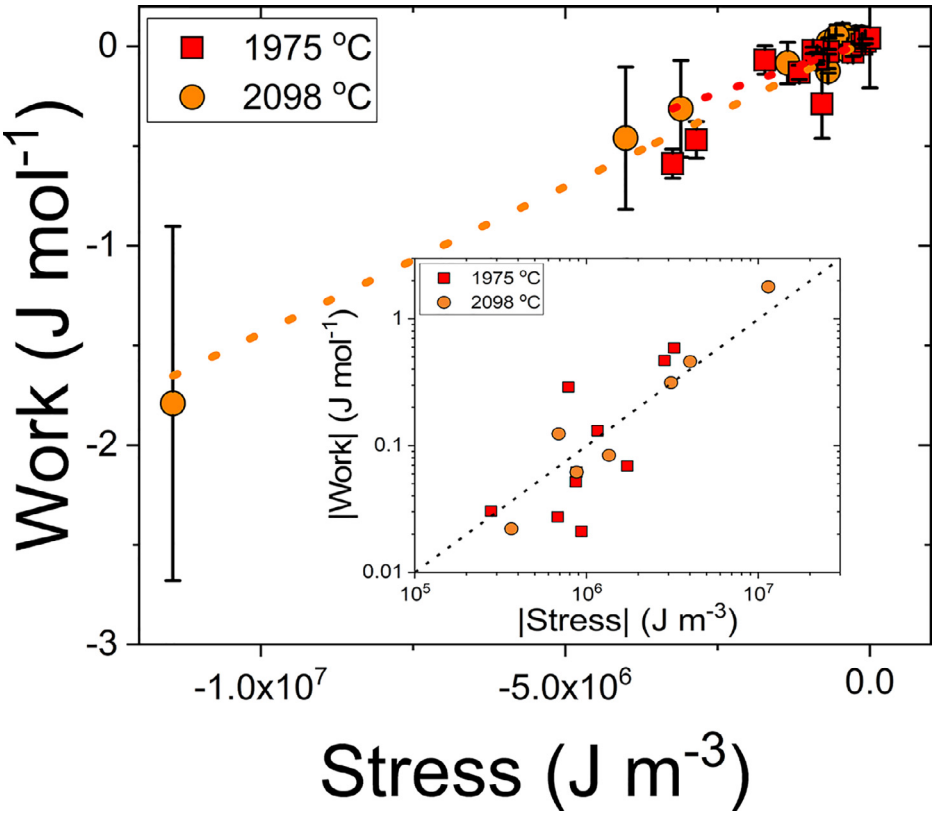

Fig. 5. The work dissipated during the constant load experiments. The main contribution to the error is the uncertainty in the zero value of the load, which is taken as ≈10x the experimental measurement sensitivity. The inset shows the absolute values of the same data on a log-log plot demonstrating that the trend is reasonably linear.

The mechanism for creep described here, grain boundary point defect diffusion to and from GBD sources and sinks, remains active down to zero average stress. Thus, it is concluded that this mechanism accounts for atomic diffusion in the grain boundary during the sintering process and likely during tracer diffusion. The activation volume, $v^* = v^f + v^m$, is the sum of the formation volume and the migration volume [81]. This implies that $v^m \approx 5.2\vec{b}^3$, since the formation volume is negligible in the total activation volume. Zn tracer diffusion measurements in a series of Al bicrystal boundaries observed an activation volume $v^* \approx 0.03\vec{b}^3 - 0.05\vec{b}^3$, or 0.26Ω to 0.39Ω, which generally agrees with a simple localized vacancy mechanism [41]. The large value observed in cubic ZrO_2, $v^m \approx 5.2\vec{b}^3$, suggests that the mass transport mediating defect is more delocalized.

The migration volume may also be described as resulting from enthalpic and entropic contributions; $v^m = v^{m,S} + v^{m,H}$ where $v^{m,H} = (\frac{\partial H}{\partial P})_T$ and $v^{m,S} = -T(\frac{\partial S}{\partial P})_T = T(\frac{\partial V}{\partial T})_P$. The thermal expansion coefficient of the activation volume should similarly be dominated by the migration contribution; $\beta^{v^m} \approx \beta^{v^*} = 7.1x10^{-3}K^{-1}$; see Figure S7. This implies that $v^{m,S} \approx 14.7\vec{b}^3$ and $v^{m,H} \approx -7.6\vec{b}^3$. The radius of the migration volume, ρ^m, under the assumption of a spherical affected volume can be also described in terms of its entropic and enthalpic contributions; $\rho^{m,S} \approx 1.5\vec{b}$ and $\rho^{m,H} \approx -1.2\vec{b}$. The relatively large migration volume is hypothesized to arise from the electrostatic interactions between bound defects, and thus the migration volume enthalpy will be dominated by electrostatic interactions. It is noted, for example, that the distance between the peak in excess charge at the boundary and depleted charge adjacent to the boundary is ≈ 0.5 nm, see Fig. 6, and that this distance is comparable to the radius of the activation volume $\rho^* \approx 0.5$ nm. It has been speculated that bound point defect clusters could explain the relative insensitivity of Al_2O_3 cation lattice and grain boundary diffusivity to aliovalent doping [82,83]. Multiple interpretations of the migration volume, however, could exist. For example, molecular dynamics simulations of MgO twist boundary suggest vacancies delocalize within the boundary plane [45]. It is likely that atomistic simulations will be necessary to identify all of the species interacting during the vacancy migration process, and that experimental data of the current type could be useful for validation.

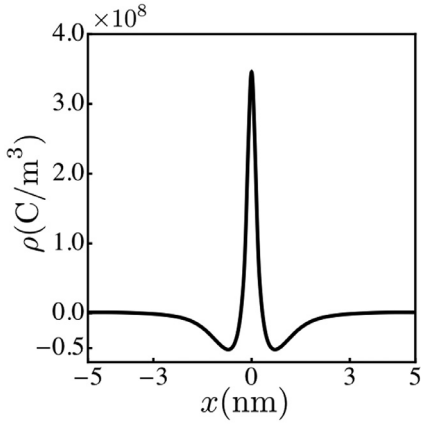

Fig. 6. Equilibrium charge density distribution in the vicinity of the grain boundary for 10% ScSZ, for a selected crystallographic misorientation, $\Delta\theta = 22.5°$. The grain boundary core is positively charged due to excess $[V_O^{\cdot\cdot}]$, which induces a negative space charge region ≈0.5 nm away from the interface and has an extent of ≈2.3 nm.

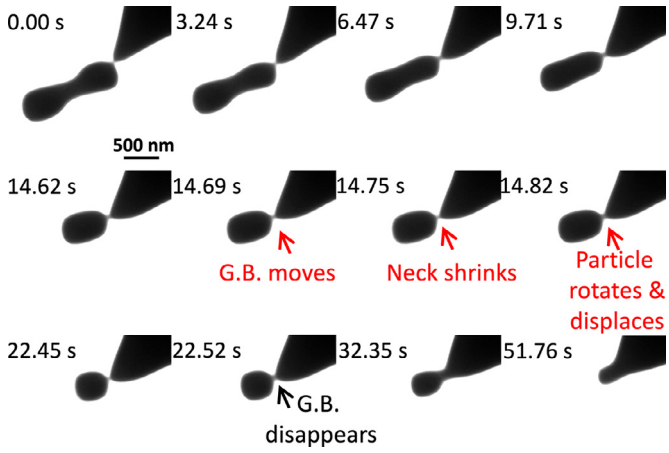

Fig. 7. Time-lapse images associated with a ScSZ particle sintering to a ScSZ substrate at 1851 °C. The particle initially contains a grain boundary, but through a series of discrete rotation and displacement events reorients into a single crystal.

3.4. Sintering and grain growth of single particles on ScSZ

Fig. 7 and Video S7 present a 'model' two-particle sintering geometry. Although, numerous *in situ* TEM observations of sintering have been reported, [25,84–89] most studies have analyzed particles sintering while also resting on substrate that can impose a considerable constraint on their evolution. The geometries analyzed here are described as 'models' for two-particle sintering because they contain one crystal that is constrained serving as the 'substrate' and a second particle that rests on this substrate that is unconstrained, other than by the grain boundary. The experiments are somewhat analogous to sintering of nanoparticles on substrates, where particles have been observed, in plan view, to be free to rotate during sintering [90].

The data in Fig. 7 support the postulate that discrete GBD formation and propagation events occur in ZrO_2 grain boundaries. Shown here is a particle remaining on the sample after a mechanical test performed at 1851 °C. The initial ≈3 sec of the experiment appears to be dominated by grain boundary migration and this process will not be discussed in detail. As shown below, the boundary velocity is sensitive to drag by the dihedral angles, making quantitative analysis challenging. Subsequent evolution of the particle appears to be dominated by surface diffusion mediated coarsening and densification. As the particle sinters, a series of discrete displacements and rotations of the particle are observed. After a series of such events the grain boundary between the particle and substrate disappears forming a single crystal. In the sequence shown, the particle rotates about the visible axis by ≈ 12 °. Fig. 8 plots the particle position, grain boundary neck position, particle size, relative geometric orientation of the particle, average dihedral angles, sintering potential, and sintering stress. The discrete displacement events cause the particle's center of mass to move towards the 'substrate', which represents densification in this geometry. The discrete densification events imply that these processes occur by the propagation of steps of a certain height through the boundary. The rotation during densification implies that this step also has an associated Burger's vector. Thus, it is hypothesized that these densification events are mediated by GBD motion. For example, disconnections are grain boundary defects of step height, h, and Burger's vector, $\vec{b}$ that could account for the phenomenon. The motion of disconnections with Burger's vectors lying in the grain boundary plane can mediate grain growth while those with Burger's vectors lying out of the grain boundary plane will have a climb component [91].

Classical models for sintering typically assume continuous diffusion in both coarsening and densification [92,93]. The neck width in our experiments generally increases with time as expected for two-particle sintering (see Fig. 8B), but transient decreases in neck width also occur that suggest the process is not continuous. As shown in Fig. 8C, these transients are also associated with discrete rotation events that also correlate with an average decrease in the dihedral angle. Fig. 8D plots the evolution of sintering potential with time. The analysis here assumes the system is isotropic, axially symmetric, and follows Josell's formulation [47] to define the relative curvature and γ_{gb}/γ_s. The details of the geometric analysis of the images are outlined in Figure S8. Although these assumptions could introduce some systematic errors, the data provide useful insights into the evolution of the particle thermodynamics. For example, the data show that the sintering potential decreases markedly just before the rotation events. The values calculated for the same geometry, but under the assumptions that $\Theta = 0$ and $\Theta = \pi$, i.e. non-wetting and zero grain boundary energy, are plotted for reference. The sintering potential is the amount of energy reduction per unit change in length due to densification. Thus, the sintering potential decreases with increasing grain boundary energy.

Just prior to the rotation events, the center of mass of the particle moves away from the boundary and the boundary width decreases, which both suggest a dewetting-like behavior consistent with an increase in the apparent boundary energy calculated from the Herring condition as shown in Figure S9A. It is referred to as an apparent grain boundary energy, since the Herring condition assumes local equilibrium. A kinetic analysis is provided below to support this assumption. Prior *in situ* measurements of two-particle MgO sintering reported similar growth of a neck followed by shrinkage of the neck and complete 'de-sintering' [89]. These particles were, however, sintered on a Si substrate that likely constrained the ability of the particles to rotate in a manner similar to the current observations. The rotation events subsequently lead to larger displacements of the particle's center of mass toward the boundary, which is attributed to densification. The experimental observations are counter-intuitive, since the transient decreases in driving force correlate with increases in the densification rate. This is indicative of the system overcoming an energy barrier. The nucleation and propagation of the GBD through the interface is indeed anticipated to have an activation barrier. The average work required to add a plane of atoms to the grain boundary during creep was found to follow $\delta w_d = v^f d\sigma$. If the formation volume is similar in compression and tension, then a similar work term should be relevant to sintering. The work available for sintering is generally $\delta w_s = \Omega d\sigma$. Under relatively simplistic conditions of constant stress and geometry, the ratio of work necessary for sintering, w_d, to the work available for sintering, w_s, would be $\frac{w_d}{w_s} = \frac{v_f}{\Omega} \approx 0.5$. The sintering potential provides evidence for such a barrier. The reduction in energy of the system associated with densification should be given by $\delta G = \Sigma dL$ for a constant Σ. Although Σ varies in the transient, the values before and after the transient are similar. Since Gibbs free energy, G, is a state-function, the change in energy is then approximately$\Delta G = \bar{\Sigma}\Delta L_1$, where $\bar{\Sigma}$ is the average of Σ before and after the transient. The densification events occur over ≈1-2 frames of the image sequence and at significantly reduced sintering potentials, $\Sigma = \Sigma_d$, and produce a displacement, ΔL_2. This displacement is approximately equivalent to that observed between the two more stable conditions before and after the transient; i.e. $\Delta L_2 = \Delta L_1$. The difference between this value, Σ_d, and those sintering potentials in the relatively stable periods before and after the event, $\bar{\Sigma}$, should approximate the work that must be done to overcome the barrier; i.e. $\Delta w_d \approx (\bar{\Sigma} - \Sigma_d)\Delta L$. The maximum energy available to do work

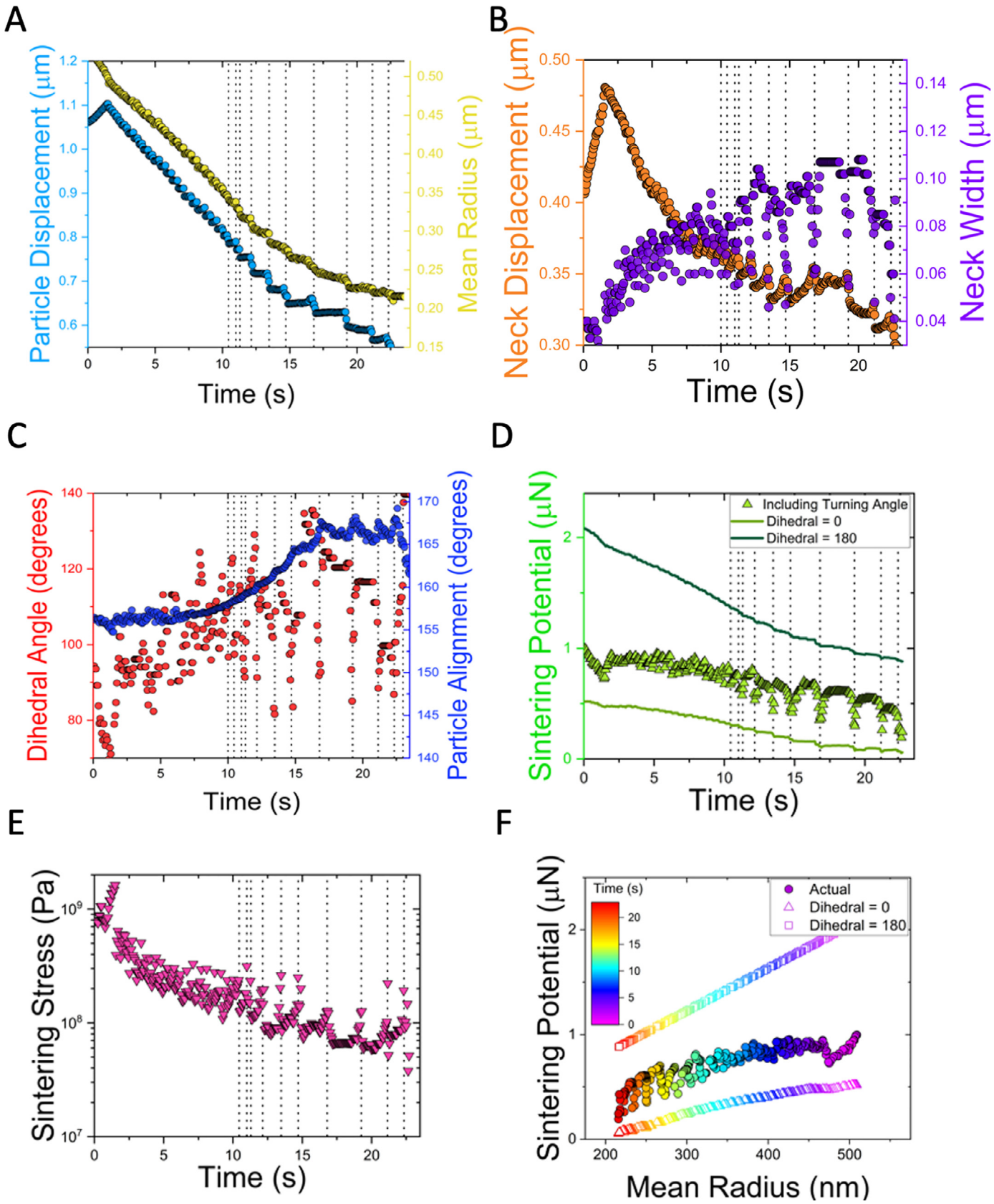

Fig. 8. A) Plots the center of mass and area of the small particle shown in Figure 4 as a function of time. B) plots the displacement of the neck position and the neck width as a function of time. C) plots the dihedral angle averaged from the two sides of the neck and the geometric orientation of the particle as a function of time. D) Plots the sintering potential of the small particle as a function of time assuming the turning angle is zero, i.e. no grain boundary, and using two different methods to approximate the turning angle at the triple line; 1 based on the dihedral angles and 2 based on the equivalent solid angle swept by the grain boundary. E) Plot of the sintering stress versus time calculated from the sintering potential and neck radius. F) The sintering potential plotted versus mean radius.

is $\Delta G = \bar{\Sigma}\Delta L$, and thus the relative barrier should be $\frac{w_d}{\Delta G} \approx 1 - \frac{\Sigma_d}{\bar{\Sigma}}$. Measuring during the last 5 events that are, temporally the most clearly resolved, produces $\frac{w_d}{\Delta G} \approx 1 - \frac{\Sigma_d}{\bar{\Sigma}} = 0.47 \pm 0.06$. Based on the discussion above $\frac{w_d}{\Delta G} \approx 1 - \frac{\Sigma_d}{\bar{\Sigma}} \approx \frac{w_d}{w_s} = \frac{v_f}{\Omega} = 0.5$. The thermodynamic analyses from creep and sintering indeed agree in magnitude, although the very close agreement here is likely fortuitous. The evolution is in fact quite complex, since the neck width, stress, and geometry all vary significantly during the transients. Nevertheless, the results support the hypothesis that an energy barrier for densification exists that derives from the work associated with the defect flux.

Two additional examples of model two-particle sintering observations are provided in Figures S10-S11 and S12-13. In each case, discontinuous densification events and discrete particle rotation events are observed consistent with the two-particle sintering experiments discussed above. These additional examples are provided to highlight the generality of the phenomena. The data in Figures S10-S11 also show a low-angle grain boundary. The data in Figure S12-S13 are obtained from a near $\Sigma 3$ grain boundary, whose misorientation will be discussed in more detail below. The transient events occur in a similar fashion for these particles, where 'de-wetting' like behavior occurs prior to densification. The two densification events observed in Figures S10-S11 produce a value of $1 - \frac{\Sigma_d}{\bar{\Sigma}} = 0.35 \pm 0.11$. This generally agrees in magnitude with the measurements from Fig. 8. The particle shown sintering in Figure S12-S13, undergoes two densification events; the first associated with a small rotation and the second associated with an observable rotation of ≈45 º. The event associated with the smaller rotation produces $1 - \frac{\Sigma_d}{\bar{\Sigma}} \approx 0.45$, while the larger rotation produces $1 - \frac{\Sigma_d}{\bar{\Sigma}} \approx 0.80$. This implies that the energy barrier to this larger rotation event may be larger. The particle in Figures S12-S13 almost completely de-wets prior to a large angle rotation that follows a less pronounced rotation event occur at a lower relative sintering potential. The phenomenon is, again, hypothesized to be indicative of an energy barrier. Fig. 8E plots the sintering stress versus time that is calculated by dividing the sintering potential, which is a force in N, by the grain boundary area, assuming a circular neck. The stress data is also indicative of the presence of an activation barrier. The sintering stress at which the rotation and densification occur are of the same order as the tensile yield strengths at similar displacement rates.

The increase in apparent grain boundary energy prior to the rotation events, plotted in supplementary Figure S9A, occurs prior to the densification event and appears to initiate the sequence of events that lead to densification. It is hypothesized that this increase in energy may correlate with the nucleation of a densification mediating GBD, that is inherently non-equilibrium, and increases the relative energy of the grain boundary. Presumably, the nucleation of such GBDs is thermally activated and biased by the local stress state. Unfortunately, these experiments provide little insights into the magnitude or nature of the activation barrier for GBD nucleation. This has been investigated to some degree using molecular dynamics simulations,[94] but the relevant factors are yet to be systematically defined. The barrier to propagation of this defect, as discussed above is too large to be thermally activated. This is supported by the observation that the system geometry responds strongly to this event, as observed as partial 'de-wetting' of the particle. The analysis here suggesting that GBD nucleation during sintering has a small work term relative to its climb agrees with the analysis of the creep data, which drew the same conclusion.

The frequency of densification events in Fig. 7 is high during the early stages of the evolution as shown in Fig. 8; occurring >20% of the time. This frequency decreases as the experiment proceeds; occurring ≈2% of the time just prior to forming a single crystal. In the initial regime, the dihedral angles are more consistent with those of a general boundary, and the later events represent lower angle boundaries. The overall frequency of densification events is ≈10%, which suggests that the classical models could predict D_{gb} to about a factor of ≈10, if other geometric and thermodynamic factors were properly accounted for. A minimum instantaneous diffusivity is calculated for each densification event using Eq. (1), where the stress is the sintering stress shown in Fig. 8E. These minimum calculated diffusivity values are plotted in Figure S9F and are referred to as minimum values because the temporal resolution of the experiment could lead to an underestimation of the diffusivity. This temporal resolution may account for the apparent trend that the calculated grain boundary diffusivities increase with time despite the fact that one might expect the higher angle boundaries at earlier times to have higher diffusivities. In fact, the frame rate of the experiment is approximately equivalent to the time constant for the densification event that is calculated based on the diffusivities measured from creep. This explains why the rotation events appear to be 'discrete' in our observations. Regardless, the diffusivity measured during densification events generally match those measured from bicrystal Coble creep within experimental error, indicating the grain boundary diffusivity is consistent amongst the two experiments. In classical models, the rate of neck growth provides an alternative basis for measuring the rate limiting diffusivity; here assumed to be either grain boundary or surface diffusion. For a constant grain boundary energy, the neck width will evolve to a constant value as described by Cannon and Carter, and others [77,95]. The overall average growth of the neck throughout the experiment, see Figure S9C, is anticipated to be primarily facilitated by the reduction in grain boundary energy resulting from rotation of the particle. Overall, the neck width increases over time following scaling that is reasonably consistent with classical continuum models; see supplementary Figure S9C. Johnson [92] noted that distinguishing grain boundary and surface diffusion models via the scaling behavior is challenging. Coble's [33] initial stage model for 2-spheres follows the form;

$$r^6/_{x^2} = \frac{96\gamma_s V_m D_{gb}}{RT} t \tag{6}$$

Fitting the overall data, between ≈2 s and 21 s, to the classical initial stage model for neck growth assuming grain boundary limited kinetics yields a value of $D_{gb,fit} = 3.9x10^{-14} m^2 s^{-1}$, which is a factor of 14 lower than the values measured from the bicrystal Coble creep experiments at the same temperature, $D_{gb} = 5.5x10^{-13} m^2 s^{-1}$. This is consistent with the aforementioned observation that GBD mediated events occur ≈10% of the time and, thus, the classical models should underestimate grain boundary diffusivity in this experiment by a factor of ≈10.

Alternatively, the rate of neck growth could be interpreted in the context of surface diffusion limited kinetics. Kuczynski [96] provided a solution to this problem for a sphere on a surface;

$$r^7/_{x^3} = \frac{56\gamma_s V_m D_s a}{RT} t \tag{7}$$

where a is the surface width, which is assumed here to be approximately the Burger's vector. Fitting the overall evolution of the neck width, between ≈2 s and 21 s, produces a surface diffusivity of $D_{s,fit} = 8.0x10^{-18} m^2 s^{-1}$. This value is considerably lower than that measured from asperity smoothing experiments at the same temperature, $D_s = 8.2x10^{-12} m^2 s^{-1}$. The overall kinetics are, therefore, grain boundary limited, but with the caveat that the diffusion is not continuous, and the average neck growth is limited by particle rotation. The surface diffusion model should, however, apply well after the particle rotates into the single crystal configuration, since this configuration satisfies the model assumptions. Fit-

ting this data, as shown in Figure S9E, produces a surface diffusivity value of $D_s = 5.3x10^{-13}m^2s^{-1}$. This underestimates the average value measured from surface asperity smoothing experiments by an order of magnitude. While anisotropy may partially account for the discrepancy, it is hypothesized that the asymmetric geometry may lead to the underestimation. This is because the center of the neck, where the width is measured, moves under capillary action, which likely produces an underestimate of surface diffusivity since more atomic flux occurs than is measured from the width alone. Figures S10-S11 provide data and associated analyses for a particle that similarly rotated into a single crystal configuration. In this case, however, the neck geometry remains more ideal in terms of its position. For this particle, the neck growth kinetics match the capillary smoothing results to within a factor of 2. This indicates that when the geometric constraints of the Kaczynski model are reasonably obeyed by the system it provides a reasonable measure of the surface diffusivity for the single crystal.

Transient periods of neck growth also occur after each rotation event and can be analyzed independently. In these transients, the neck position is relatively stable on the length-scale relevant to surface diffusion. Since grain boundary diffusion mediated neck growth is discontinuous, as shown in the overall trend, the transient growth of the neck must be surface diffusion mediated. The classical model, of course, does not consider the reduction in driving force resulting from the non-zero turning angles at the triple line. Fig. 8D indicates that the driving force is reduced by less than a factor of 2 at any instance, so this term is not anticipated to have a major influence on order of magnitude of the calculated diffusivities. Most of the transient neck growth events occurring in the presence of the grain boundary exhibit sub-linear slopes over significant periods of time and decay rapidly toward zero slope. Surface diffusivities calculated from these transients are several orders of magnitude lower than the single crystal value. Both the decaying neck growth rate and underestimation of diffusivity likely reflect the tendency for the geometry to approach configurations that satisfy local equilibrium on a timescale that is fast relative to the temporal resolution of the observations. Similar rapid local equilibration of dihedral angles has been observed in phase-field simulations of 2-particle sintering where the initial dihedral angles were out-of-equilibrium [97]. The observation that surface diffusion kinetics are fast relative to those needed to satisfy local equilibrium supports the hypothesis above, and plotted in Fig. 8A, that the dihedral angles are likely close to local equilibrium.

Rotation of micron scale particles during sintering of relatively dense particle compacts and model low density geometries has been observed in several studies that utilized marker features, and x-ray tomography [98–100]. These studies suggest that GBD mediate densification likely plays a role in sintering more broadly. The current experiments suggest that GBD nucleation is not the major portion of the energy barrier. Similarly, the increase in apparent grain boundary energy prior to densification events suggests that GBD nucleation likely precedes the majority of work performed during a densification event. The nucleation rate of densification mediating GBDs could strongly influence the densification rate, but little is known about this process. It is assumed that unlike the barrier to densification, the nucleation of the GBDs is likely thermally activated and stress assisted. This leads to a situation where densification is inherently reaction-rate limited due to the kinetics being limited by the nucleation of GBDs while coarsening follows diffusion-limited kinetics. In fact, a plot of displacement rate versus sintering stress, shown in Figure S9F, produces results that are reasonably consistent with interface reaction-rate limited kinetics, where a non-linear response is observed as a function of driving force. It should be noted since the measurement includes a number of boundaries of distinct misorientation and geometry, the critical driving force is likely to be different for each boundary. It is important to note that the discussion, herein, focuses on submicron scale grain boundary widths and bicrystal geometries. Our analysis could, therefore, be restricted to situations in which either zero or one densification or creep mediating GBD exists within a grain boundary at any instance. Larger grain boundaries in which multiple densification mediating GBDs could exist may not exhibit discontinuous diffusion during densification. During sintering of multi-particle compacts stresses evolved from the displacement and rotation induced by densification events could induce stresses that cause the reaction pathway and overall evolution to depart significantly from the model two-particle observations made here.

Other microstructural evolution phenomena were also observed during relaxation of asperity geometries formed during the creep experiments. Grain boundary migration can occur in part or fully via the migration of GBDs, such as disconnections, as has been observed via *in situ* TEM and molecular dynamics simulations, and predicted by theory [38,101–103]. These GBDs, however, should have different Burger's vectors than those inducing densification, particularly with respect to whether the Burger's vector is in or out of the grain boundary plane [38]. Figures S14-S15 show several examples of sintering of single ScSZ particles on bulk ScSZ showing different behaviors in terms of grain growth and densification. The driving force for grain growth was calculated based on a 2-D analysis where the curvature of the boundary is based on measurements of the turning angle at the two triple lines and the solid angle between them and the grain's center of mass, such as discussed in reference. [104] This is approximately the application of the Mullin's-von Neumann [105] analysis to a single grain boundary under anisotropic conditions. The grain boundary mobilities measured in different experiments varied significantly and appeared to depend on the degree of pinning by surface dihedral angle grooves; i.e. the height of the surface groove ahead of the advancing boundary. For this reason, grain boundary mobilities were not analyzed in detail. Nevertheless, it is noted that in many bicrystal configurations grain growth occurred rather than densification, which is in agreement with prior observations of Cu nanoparticles on Cu substrates [90].

Figure S16 presents two examples where initially single crystalline asperities form grain boundaries due to Rayleigh instabilities that causes portions of the material to rotate rapidly. In the two examples, the rotations are associated with the formation of $\Sigma 3$ and $\Sigma 9$ tilt grain boundaries, which are twinning reactions that occur when the single crystalline neck approaches the instability. The sintering behavior of this $\Sigma 3$ was analyzed in Figures S12-S13. The $\Sigma 9$ tilt boundary in cubic ZrO_2 is a relatively low energy boundary, while the $\Sigma 3$ tilt is a relatively high energy as reported in Ref. [106]. The relevant plots were not included in Reference [106] and therefore the associated data is shown in Figure S11 for reference. The observations suggest that the formation of these boundaries may be driven more by the favorable slip and twinning conditions rather than grain boundary energy minimization. For example, the pure twist $\Sigma 3$ is significantly lower in energy than the symmetric $\Sigma 3$ tilt boundary.

Finally, the results of our model two-particle sintering experiments indicate that densification follows reaction-rate limited kinetics, at least in the particle size range characterized herein, while coarsening follows diffusion-limited kinetics. These two processes will have inherently different activation energies. This explains why relatively high activation energies for densification and relatively low activations for coarsening have been observed during sintering, which results in non-densifying processes dominating at low temperatures and densifying processes dominating at high temperatures [107]. The work in this series of papers suggests that the activation energy for surface diffusion and grain boundary diffusion are similar. This provides further understanding of how

rapid heating rates benefit densification by suppressing coarsening occurring at low temperatures during heating. Although this work focuses on a single chemistry and has been discussed in context of novel sintering temperature schedules, [9,20,22,24–28] the knowledge that densification in some cases may be interface reaction-rate limited should also become important in considering dopant effects. The effects of dopant chemistry on sintering has been a topic of ongoing research for many decades [108]. The results of associated experiments performed on oxides are typically interpreted in the context of dopant effects on point defect concentrations and interfacial diffusivities. However, the current results suggest that in some cases it may be more important to understand how dopants affect the nucleation and motion of GBDs.

4. Conclusion

The results suggest that the same mechanism controls sintering and Coble creep in cubic ZrO_2; transport of vacancies to and from GBDs. The activation, formation, and migration volumes for diffusion were all determined experimentally. The formation volume is small and positive consistent with a vacancy-type point defect formation. The activation volume, however, is quite large suggesting that the motion of the rate limiting defect is highly delocalized, possibly due to binding between charged defects. The surface and grain boundary energies were determined through what, to the authors' knowledge, is the first application of the zero-creep method to a crystalline oxide. Finally, the results indicate that an activation barrier exists to the removal of atomic planes from the grain boundary during densification, which causes densification to follow reaction rate-limited during two-particle sintering of submicron scale necks.

5. Contributions

R.L. Grosso prepared the 10ScSZ samples for testing in collaboration with E.N.S. Muccillo, D.N.F. Muche, and R.H.R. Castro, and assisted with experimental data analysis.L. Feng and G.S. Jawaharram also helped complete the experimental data analysis. C.M. Barr and A.M. Monterrosa helped perform high temperature experiments. K. Hattar and S.J. Dillon oversaw the experimental aspects of this work.K.S.N. Vikrant perfomed the reported phase-field work and associated analysis under the supervision of R.E. García.

Video S1: YSZ-ScSZ grain boundary formed at 1928 °C during *in situ* pre-annealing of 30 sec, which was then loaded in tension at a displacement rate of 40 nm s^{-1}.The field of view is 4.07 μm by 4.07 μm.

Declaration of Competing Interest

The authors declare that they have no known competing financial interests or personal relationships that could have appeared to influence the work reported in this paper.

Acknowledgements

Support from National Science Foundation under Grant No. DMR 1922867 is acknowledged by SJD. RG and EM gratefully acknowledge FAPESP (2016/06205-1 and 2017/25501-3), CAPES (Finance code 001), and CNPq (305889/2018-4) for the financial support. DM acknowledges Conselho Nacional de Desenvolvimento Científico e Tecnológico (236631/2012-8). Support from the Army Research Office Grants W911NF1810361 and W911NF1710026 are acknowledged by RC. K.S.N. Vikrant and R.E. García thank the support provided by US ONR N00014- 17-1-2087. This work was carried out in part in the Frederick Seitz Materials Research Laboratory Central Research Facilities, University of Illinois at Urbana-Champaign. CMB and KH were supported by the DOE-BES Materials Science and Engineering Division under FWP 15013170. This work was performed, in part, at the Center for Integrated Nanotechnologies, an Office of Science User Facility operated for the U.S. Department of Energy (DOE) Office of Science. Sandia National Laboratories is a multi-mission laboratory managed and operated by National Technology & Engineering Solutions of Sandia, LLC, a wholly owned subsidiary of Honeywell International, Inc., for the U.S. DOE's National Nuclear Security Administration under contract DE-NA-0003525. The views expressed in the article do not necessarily represent the views of the U.S. DOE or the United States Government. We would also like to thank Greg Rohrer for help replotting the grain boundary energy data in the supplementary information and W. Craig Carter for useful discussions.

Supplementary materials

Supplementary material associated with this article can be found, in the online version, at doi:10.1016/j.actamat.2020.08.070.

References

[1] R. Waser, R. Hagenbeck, Grain boundaries in dielectric and mixed-conducting ceramics, Acta Mater. 48 (4) (2000) 797–825.
[2] A.H. Heuer, Oxygen and aluminum diffusion in α-Al2O3: How much do we really understand? J. Eur. Ceram. Soc. 28 (7) (2008) 1495–1507.
[3] P.R. Cantwell, et al., Grain boundary complexions, Acta Mater. 62 (2014) 1–48.
[4] G.S. Rohrer, Measuring and interpreting the structure of grain-boundary networks, J. Am. Ceram. Soc. 94 (3) (2011) 633–646.
[5] M. Baeurer, et al., Grain growth anomaly in strontium titanate, Scr. Mater. 61 (6) (2009) 584–587.
[6] E.A. Holm, S.M. Foiles, How grain growth stops: A mechanism for grain–growth stagnation in pure materials, Science (Washington, DC, U. S.) 328 (5982) (2010) 1138–1141.
[7] D.L. Olmsted, S.M. Foiles, E.A. Holm, Grain boundary interface roughening transition and its effect on grain boundary mobility for non-faceting boundaries, Scr. Mater. 57 (12) (2007) 1161–1164.
[8] V. Tikare, et al., Comparison of phase-field and Potts models for coarsening processes, Acta Mater. 47 (1) (1998) 363–371.
[9] R. Raj, M. Cologna, J.S.C. Francis, Influence of externally imposed and internally generated electrical fields on grain growth, diffusional creep, sintering and related phenomena in ceramics, J. Am. Ceram. Soc. 94 (7) (2011) 1941–1965.
[10] Z. Shen, et al., Spark plasma sintering of alumina, J. Am. Ceram. Soc. 85 (8) (2002) 1921–1927.
[11] R.M. Cannon, W.H. Rhodes, A.H. Heuer, Plastic deformation of fine-grained alumina (Al2O3): I, interface-controlled diffusional creep, J. Am. Ceram. Soc. 63 (1-2) (1980) 46–53.
[12] Y.-Z. Li, et al., Codoping of alumina to enhance creep resistance, J. Am. Ceram. Soc. 82 (6) (1999) 1497–1504.
[13] H. Yoshida, Y. Ikuhara, T. Sakuma, Grain boundary electronic structure related to the high-temperature creep resistance in polycrystalline Al2O3, Acta Mater. 50 (11) (2002) 2955–2966.
[14] O.A. Ruano, J. Wadsworth, O.D. Sherby, Deformation of fine-grained alumina by grain boundary sliding accommodated by slip, Acta Mater. 51 (12) (2003) 3617–3634.
[15] M.W. Finnis, A.Y. Lozovoi, A. Alavi, The oxidation of NiAl: What can we learn from ab initio calculations? Annu. Rev. Mater. Res. 35 (2005) 167–207 4 plates.
[16] B.A. Pint, Optimization of reactive-element additions to improve oxidation performance of alumina-forming alloys, J. Am. Ceram. Soc. 86 (4) (2003) 686–695.
[17] A.H. Heuer, et al., On the growth of Al2O3 scales, Acta Mater. 61 (18) (2013) 6670–6683.
[18] A.H. Heuer, M. Zahiri Azar, A disconnection mechanism of enhanced grain boundary diffusion in Al2O3, Scr. Mater. 102 (2015) 15–18.
[19] L. Zhang, et al., Equation of motion for a grain boundary, Phys. Rev. Lett. 119 (24) (2017) p. 246101/1-246101/5.
[20] M. Cologna, B. Rashkova, R. Raj, Flash sintering of nanograin zirconia in <5 s at 850°C, J. Am. Ceram. Soc. 93 (11) (2010) 3556–3559.
[21] J. Guo, et al., Cold Sintering: A Paradigm Shift for Processing and Integration of Ceramics, Angewandte Chemie International Edition 55 (38) (2016) 11457–11461.
[22] S.K. Jha, et al., The effects of external fields in ceramic sintering, J. Am. Ceram. Soc. 102 (1) (2019) 5–31.
[23] M.P. Harmer, R.J. Brook, Fast firing - microstructural benefits, Trans. J. Br. Ceram. Soc. 80 (5) (1981) 147–149.
[24] R. Roy, et al., Full sintering of powdered-metal bodies in a microwave field, Nature (London) 399 (6737) (1999) 668–670.

[25] H. Majidi, T.B. Holland, K. van Benthem, Quantitative analysis for in situ sintering of 3% yttria-stabilized zirconia in the transmission electron microscope, Ultramicroscopy 152 (2015) 35–43.
[26] C. Wang, et al., A general method to synthesize and sinter bulk ceramics in seconds, Science 368 (6490) (2020) 521.
[27] Y. Zhang, et al., Probing the densification mechanisms during flash sintering of ZnO, Acta Materialia 125 (2017) 465–475.
[28] W. Ji, et al., Ultra-fast firing: Effect of heating rate on sintering of 3YSZ, with and without an electric field, J. Eur. Ceram. Soc. 37 (6) (2017) 2547–2551.
[29] Vikrant, K.S.N., et al., Ultrahigh Temperature in situ Transmission Electron Microscopy based Bicrystal Coble Creep in Zirconia I: Nanowire Growth and Interfacial Diffusivity. Submitted.
[30] R.L. Grosso, et al., Ionic conductivity and phase stability of spark plasma sintered scandia and ceria-stabilized zirconia, Solid State Ionics 230 (2013) 48–51.
[31] S.G. Huang, et al., Microwave sintering of CeO2 and Y2O3 co-stabilised ZrO2 from stabiliser-coated nanopowders, J. Eur. Ceram. Soc. 27 (2) (2007) 689–693.
[32] H.E. Exner, C. Müller, Particle Rearrangement and Pore Space Coarsening During Solid-State Sintering, J. Am. Ceram. Soc. 92 (7) (2009) 1384–1390.
[33] R.L. Coble, Initial Sintering of Alumina and Hematite, J. Am. Ceram. Soc. 41 (2) (1958) 55–62.
[34] K. Kolluri, M.J. Demkowicz, Dislocation mechanism of interface point defect migration, Phys. Rev. B 82 (19) (2010) 193404.
[35] M.F. Ashby, On interface-reaction control of Nabarro-Herring creep and sintering, Scripta Metallurgica 3 (11) (1969) 837–842.
[36] S. Mao, et al., Quantitative comparison of sink efficiency of Cu–Nb, Cu–V and Cu–Ni interfaces for point defects, Acta Materialia 82 (2015) 328–335.
[37] A.H. King, D.A. Smith, On the mechanisms of point-defect absorption by grain and twin boundaries, Philos. Mag. A 42 (4) (1980) 495–512.
[38] J. Han, S.L. Thomas, D.J. Srolovitz, Grain-boundary kinetics: A unified approach, Progr. Mater. Sci. 98 (2018) 386–476.
[39] Z. He, J. Ma, Constitutive modelling of the densification of micron-grain-sized alumina ceramics, Philos. Mag. 83 (16) (2003) 1889–1916.
[40] J. Croquesel, et al., Direct microwave sintering of pure alumina in a single mode cavity: Grain size and phase transformation effects, Acta Mater. 116 (2016) 53–62.
[41] P. Klugkist, et al., Diffusion of Zn along tilt grain boundaries in Al: pressure and orientation dependence, Acta Mater. 49 (15) (2001) 2941–2949.
[42] W. Lojkowski, et al., The effect of pressure on indium diffusion along <001>tilt grain boundaries in copper bicrystals, Interface Sci. 6 (3) (1998) 187–196.
[43] Y. Tamura, et al., Grain-boundary diffusion coefficient in α-Al2O3 from spark plasma sintering tests: Evidence of collective motion of charge disconnections, Ceram. Int. 44 (15) (2018) 19044–19048.
[44] R.L. Coble, A Model for Boundary Diffusion Controlled Creep in Polycrystalline Materials, J. Appl. Phys. 34 (6) (1963) 1679–1682.
[45] K. Kolluri, E. Martinez Saez, B.P. Uberuaga, Structure and Mobility of Dissociated Vacancies at Twist Grain Boundaries and Screw Dislocations in Ionic Rocksalt Compounds, Chem. Mater. 30 (6) (2018) 1980–1988.
[46] R.C. Koeller, H.G. Drickamer, The effect of pressure on self-diffusion in carbon disulfide, J. Chem. Phys. 21 (1953) 267–273.
[47] D. Josell, Exact solution for the zero creep load of a wire, Acta Metallurgica et Materialia 41 (7) (1993) 2179–2183.
[48] H. Udin, A.J. Shaler, J. Wulff, The surface tension of solid copper, JOM 1 (2) (1949) 186–190.
[49] R.L. Grosso, E.N.S. Muccillo, R.H.R. Castro, Phase stability in scandia-zirconia nanocrystals, J. Am. Ceram. Soc. 100 (5) (2017) 2199–2208.
[50] R.L. Grosso, et al., Sintering of translucent and single-phase nanostructured scandia-stabilized zirconia, Mater. Lett. 253 (2019) 246–249.
[51] J.-M. Costantini, F. Beuneu, Threshold displacement energy in yttria-stabilized zirconia, Physica Status Solidi C 4 (3) (2007) 1258–1263.
[52] A. Fitzgibbon, M. Pilu, R.B. Fisher, Direct least square fitting of ellipses, IEEE Trans. Pattern Anal. Mach. Intel. 21 (5) (1999) 476–480.
[53] Grosso, R.L., et al., In situ Transmission Electron Microscopy for Ultrahigh Temperature Mechanical Testing of ZrO2. Nano Lett. 20: p. 1041-1046.
[54] D. Kiener, et al., In situ nanocompression testing of irradiated copper, Nat. Mater. 10 (8) (2011) 608–613.
[55] N. Shibata, et al., Grain-boundary faceting at a = 3, [110]/{112} grain boundary in a cubic zirconia bicrystal, Philos. Mag. 83 (19) (2003) 2221–2246.
[56] H. Yoshida, et al., High-temperature grain boundary sliding behavior and grain boundary energy in cubic zirconia bicrystals, Acta Mater. 52 (8) (2004) 2349–2357.
[57] M. Kawasaki, et al., Atomic control of the SrTiO3 crystal surface, Science (Washington, D. C.) 266 (5190) (1994) 1540–1542.
[58] M. Yoshimoto, et al., Atomic-scale formation of ultrasmooth surfaces on sapphire substrates for high-quality thin-film fabrication, Appl. Phys. Lett. 67 (18) (1995) 2615–2617.
[59] B. Burton, Interface reaction controlled diffusional creep: A consideration of grain boundary dislocation climb sources, Mater. Sci. Eng. 10 (1972) 9–14.
[60] A. Villani, E.P. Busso, S. Forest, Field theory and diffusion creep predictions in polycrystalline aggregates, Model. Simul. Mater. Sci. Eng. 23 (5) (2015) 055006.
[61] M. Magri, et al., A coupled model of diffusional creep of polycrystalline solids based on climb of dislocations at grain boundaries, J. Mech. Phys. Solids 135 (2020) 103786.
[62] Y. Mishin, et al., Irreversible thermodynamics of creep in crystalline solids, Phys. Rev. B 88 (18) (2013) 184303.
[63] A.G. Evans, R.D. Rawlings, Thermally activated deformation of crystalline materials, Phys. Status Solidi 34 (1) (1969) 9–31.
[64] R.J. Asaro, S. Suresh, Mechanistic models for the activation volume and rate sensitivity in metals with nanocrystalline grains and nano-scale twins, Acta Mater. 53 (12) (2005) 3369–3382.
[65] M. Koncztkowski, D. Lesueur, J. Dural, The measurement of the activation volume of interstitials in electron irradiated platinum, Rad. Effects 43 (2) (1979) 65–68.
[66] L. Kornblit, Self-diffusion entropies and activation volumes in fcc metals, Physica B+C 113 (2) (1982) 169–174.
[67] F. Bejina, et al., Activation volume of silicon diffusion in San Carlos olivine, Geophys. Res. Lett. 24 (21) (1997) 2597–2600.
[68] S.B. Jung, et al., Activation volumes for diffusion of copper, iron and silicon in nickel, J. Mater. Sci. Lett. 12 (13) (1993) 1057–1058.
[69] U. Soedervall, M. Friesel, A. Lodding, Atomic transport of trivalent impurities in silicon: diffusion, isotope effects, activation volumes, J. Chem. Soc., Faraday Trans. 86 (8) (1990) 1293–1298.
[70] M.J. Kobrinsky, C.V. Thompson, Activation volume for inelastic deformation in polycrystalline Ag thin films, Acta Materialia 48 (3) (2000) 625–633.
[71] Q. Wei, et al., Effect of nanocrystalline and ultrafine grain sizes on the strain rate sensitivity and activation volume: fcc versus bcc metals, Mater. Sci. Eng. A 381 (1) (2004) 71–79.
[72] T.J. Rupert, J.C. Trenkle, C.A. Schuh, Enhanced solid solution effects on the strength of nanocrystalline alloys, Acta Materialia 59 (4) (2011) 1619–1631.
[73] A.T. Jennings, J. Li, J.R. Greer, Emergence of strain-rate sensitivity in Cu nanopillars: Transition from dislocation multiplication to dislocation nucleation, Acta Materialia 59 (14) (2011) 5627–5637.
[74] O.D. Sherby, J.L. Robbins, A. Goldberg, Calculation of Activation Volumes for Self-Diffusion and Creep at High Temperature, J. Appl. Phys. 41 (10) (1970) 3961–3968.
[75] T. Zhu, et al., Temperature and Strain-Rate Dependence of Surface Dislocation Nucleation, Phys. Rev. Lett. 100 (2) (2008) 025502.
[76] L. Smith, D. Farkas, Deformation response of grain boundary networks at high temperature, J. Mater. Sci. 53 (8) (2018) 5696–5705.
[77] R.M. Cannon, W.C. Carter, Interplay of Sintering Microstructures, Driving Forces, and Mass Transport Mechanisms, J. Am. Ceram. Soc. 72 (8) (1989) 1550–1555.
[78] C. Herring, Some Theorems on the Free Energies of Crystal Surfaces, Phys. Rev. 82 (1) (1951) 87–93.
[79] A. Tsoga, P. Nikolopoulos, Surface and grain-boundary energies in yttria-stabilized zirconia (YSZ-8 mol%), J. Mater. Sci. 31 (20) (1996) 5409–5413.
[80] G.C.C. Costa, et al., Calorimetric Measurement of Surface and Interface Enthalpies of Yttria-Stabilized Zirconia (YSZ), Chem. Mater. 22 (9) (2010) 2937–2945.
[81] M.J. Aziz, Thermodynamics of diffusion under pressure and stress: relation to point defect mechanisms, Appl. Phys. Lett. 70 (21) (1997) 2810–2812.
[82] L. Feng, S.J. Dillon, Cation grain-boundary diffusivity in SiO2- and MgO-doped Al2O3, J. Am. Ceram. Soc. 100 (12) (2017) 5379–5384.
[83] L. Feng, S.J. Dillon, Cr3+ chemical diffusivity in aliovalent doped aluminas, J. Eur. Ceram. Soc. 37 (13) (2017) 4025–4032.
[84] J. Rankin, B.W. Sheldon, In situ TEM sintering of nano-sized ZrO2 particles, Mater. Sci. Eng. A A204 (1–2) (1995) 48–53.
[85] J. Rankin, L.A. Boatner, Unstable neck formation during initial-stage sintering, J. Am. Ceram. Soc. 77 (8) (1994) 1987–1990.
[86] R.-J. Liu, et al., In situ electron microscopy studies of the sintering of palladium nanoparticles on alumina during catalyst regeneration processes, Microsc. Microanal. 10 (1) (2004) 77–85.
[87] A.T. DeLaRiva, et al., In situ transmission electron microscopy of catalyst sintering, J. Catal. 308 (2013) 291–305.
[88] S.R. Challa, et al., Relating Rates of Catalyst Sintering to the Disappearance of Individual Nanoparticles during Ostwald Ripening, J. Am. Chem. Soc. 133 (51) (2011) 20672–20675.
[89] J. Rankin, L.A. Boatner, Unstable Neck Formation during Initial-Stage Sintering, J. Am. Ceram. Soc. 77 (8) (1994) 1987–1990.
[90] M. Yeadon, et al., In-situ observations of classical grain growth mechanisms during sintering of copper nanoparticles on (001) copper, Appl. Phys. Lett. 71 (12) (1997) 1631–1633.
[91] J.P. Hirth, R.W. Balluffi, On grain boundary dislocations and ledges, Acta Metallurgica 21 (7) (1973) 929–942.
[92] D.L. Johnson, I.B. Cutler, Diffusion Sintering: I, Initial Stage Sintering Models and Their Application to Shrinkage of Powder Compacts, J. Am. Ceram. Soc. 46 (11) (1963) 541–545.
[93] R.L. Coble, Sintering Crystalline Solids. II. Experimental Test of Diffusion Models in Powder Compacts, J. Appl. Phys. 32 (5) (1961) 793–799.
[94] J.M. Sestito, et al., An atomistic simulation study of nanoscale sintering: The role of grain boundary misorientation, Comput. Mater. Sci. 165 (2019) 180–189.
[95] F.F. Lange, Densification of powder compacts: An unfinished story, J. Eur. Ceram. Soc. 28 (7) (2008) 1509–1516.
[96] G.C. Kuczynski, Self-diffusion in sintering of metallic particles, Trans. Am. Inst. Min., Metall. Pet. Eng. 1 (No. 2, Trans.) (1949) 169–178.
[97] F. Abdeljawad, et al., Sintering processes in direct ink write additive manufacturing: A mesoscopic modeling approach, Acta Materialia 169 (2019) 60–75.

[98] B. Kieback, et al., Analysis of particle rolling and intrinsic rotations in copper powder during sintering, J. Mater. Sci. 47 (20) (2012) 7047–7055.
[99] F. Wakai, et al., Direct observation of sintering mechanics of a single grain boundary, Acta Materialia 60 (2) (2012) 507–516.
[100] S.A. McDonald, et al., Microstructural evolution during sintering of copper particles studied by laboratory diffraction contrast tomography (LabDCT), Sci. Rep. 7 (1) (2017) 5251.
[101] Q. Zhu, et al., In situ atomistic observation of disconnection-mediated grain boundary migration, Nat. Commun. 10 (1) (2019) 156.
[102] S.E. Babcock, R.W. Balluffi, Grain boundary kinetics—I. In situ observations of coupled grain boundary dislocation motion, crystal translation and boundary displacement, Acta Metallurgica 37 (9) (1989) 2357–2365.
[103] S.E. Babcock, R.W. Balluffi, Grain boundary kinetics—II. In situ observations of the role of grain boundary dislocations in high-angle boundary migration, Acta Metallurgica 37 (9) (1989) 2367–2376.
[104] S.J. Dillon, G.S. Rohrer, Mechanism for the development of anisotropic grain boundary character distributions during normal grain growth, Acta Materialia 57 (1) (2009) 1–7.
[105] W.W. Mullins, Two-Dimensional Motion of Idealized Grain Boundaries, J. Appl. Phys. 27 (8) (1956) 900–904.
[106] L. Helmick, et al., Crystallographic Characteristics of Grain Boundaries in Dense Yttria-Stabilized Zirconia, Int. J. Appl. Ceram. Tech. 8 (5) (2011) 1218–1228.
[107] M.-Y. Chu, et al., Effect of Heating Rate on Sintering and Coarsening, J. Am. Ceram. Soc. 74 (6) (1991) 1217–1225.
[108] S.J. Bennison, M.P. Harmer, A history of the role of magnesia in the sintering of α-alumina, Ceram. Trans. 7 (Sintering Adv. Ceram.) (1990) 13–49.